Industrial Chemistry & Materials

ROYAL SOCIETY OF CHEMISTRY

PAPER

View Article Online
View Journal | View Issue

Cite this: *Ind. Chem. Mater.*, 2025, **3**, 203

Rational design of a carbon nitride photocatalyst with in-plane electron delocalization for photocatalytic hydrogen evolution†

Quanguo Hao, *[a] Yuhua Zhu,[b] Yuan Li,[c] Zhenhua Li,*[d] Hong Yuan [c] and Shuxin Ouyang[c]

Received 19th September 2024,
Accepted 31st October 2024

DOI: 10.1039/d4im00118d

rsc.li/icm

Photocatalytic hydrogen evolution based on the use of carbon nitride (CN) catalyst offers a sustainable route to convert solar energy into hydrogen energy; however, its activity is severely restricted by the sluggish transfer of photogenerated charges. Herein, we report a novel approach involving boron (B) doping-induced π-electron delocalization in CN for efficient hydrogen (H_2) evolution. The as-prepared B-doped CN (BCN) catalyst presented an 8.6-fold enhancement in the H_2-evolution rate (7924.0 μmol h^{-1} g^{-1}) under visible-light irradiation compared with pristine CN, which corresponded to an apparent quantum yield (AQY) of 14.5% at 405 nm. Experimental analysis and density functional theory (DFT) calculations demonstrated that B doping induced π-electron delocalization in conjugated CN rings to generate a new intermediate state within the band gap to provide a new transfer path for visible-light utilization, thus achieving the high separation and transfer of photoinduced carriers. This work provides a new approach to adjust the electronic structure of CN-like conjugated polymer semiconductors for efficient catalytic energy conversion.

Keywords: B doping; π-electron delocalization; H_2 evolution; Photocatalysis.

1 Introduction

Converting a constant stream of solar energy into green hydrogen energy is a promising solution to tackle the impending world energy crisis.[1–4] Direct photocatalytic water splitting into hydrogen (H_2) under visible-light irradiation using a highly efficient photocatalyst is an available approach.[5,6] To date, various classical photocatalysts, such as CdS, Fe_2O_3, ZnO, WO_3, and TiO_2, have been developed to pursue this goal.[7] However, the above photocatalysts still have some inherent shortcomings, such as instability, weak redox capacity and narrow absorption spectrum, and therefore cannot meet practical applications.[8] Compared with these photocatalysts, metal-free carbon nitride (CN) possesses high thermal and chemical stability and an adjustable electronic structure, which give it wide prospects in the field of photocatalytic H_2 evolution.[9–11] Moreover, the solid yields of carbon nitride synthesis can be easily enhanced by introducing binapthyl organic groups or some inorganics, such as salts or silicotungstic acid,[11,12] which can meet the needs of industrial development. However, pristine CN presents narrow visible-light absorption, low charge mobility, and a high recombination of photogenerated electron–hole (e^-–h^+) pairs under working conditions, which depress its photocatalytic H_2-evolution activity.[13–16] In particular, the sluggish transfer of photocarriers results in the transient recombination of photoinduced e^-–h^+ pairs inside and on the surface of CN, which severely affects their utilization efficiency. Some studies have found that introducing electron delocalization into the microstructure of catalysts forms built-in electric field, which contributes to high charge-carrier mobility.[17,18] Therefore, introducing an intrinsic driving force into the π-conjugated units of CN could promote electron delocalization around photoexcitation sites to achieve the swift mobility of photoinduced carriers.

As a typical approach, introducing heteroatoms to modulate the electronic structure of CN has been attempted to promote π-electron delocalization, achieving a high

[a] *National Centre for Magnetic Resonance in Wuhan, State Key Laboratory of Magnetic Resonance and Atomic and Molecular Physics, Innovation Academy for Precision Measurement Science and Technology, Chinese Academy of Sciences, Wuhan 430071, China. E-mail: haoquanguo@apm.ac.cn*
[b] *School of Civil Engineering, Wuhan University, No. 8, East Lake South Road, Wuhan 430072, China*
[c] *Key Laboratory of Pesticide and Chemical Biology of Ministry of Education, College of Chemistry, Central China Normal University, Wuhan 430079, China*
[d] *Key Laboratory of Photochemical Conversion and Optoelectronic Materials, Technical Institute of Physics and Chemistry, Chinese Academy of Sciences, Beijing 100190, China. E-mail: lizhenhua@mail.ipc.ac.cn*

† Electronic supplementary information (ESI) available. See DOI: https://doi.org/10.1039/d4im00118d

utilization of photogenerated carriers.[19–21] This solution is predominantly based on two key factors: 1) the adjustable band structure of CN, which provides the possibility of broadening the range of visible-light absorption,[22,23] and 2) nonmetallic bonds in π-conjugated units in the in-plane direction, which allow easy doping of other elements or functional groups for providing more reactive sites, such as a micro-π-conjugated connection unit or nonmetallic elements (*e.g.*, P, B, Br, I, and S).[24–29] It is worth noting that boron (B), with a similar atomic radius as C or N, has a great extent of miscibility in the CN framework. However, the electronegativity of B (2.05) is different from that of N (3.04) and C (2.55).[30] The introduction of B atoms can rearrange the chemical structure or modulate the electronic structure of the CN framework and even act as adsorption sites for the reactant molecules.[31–33] Encouraged by these advantages, some researchers have reported that B-doping can promote electronic redistribution at the interface to build an interfacial charge-transfer channel for the improved utilization of photoinduced carriers, which can promote enhanced photocatalytic activities.[34,35] However, B-doping-induced π-electron delocalization in the conjugated CN and its promotion mechanism for highly efficient photocatalytic hydrogen evolution have not been elucidated yet.

Herein, we prepared a BCN photocatalyst, which could realize effective photocatalytic H_2 evolution. Under visible-light irradiation, the as-prepared BCN showed a much-improved photocatalytic H_2 evolution rate of 7924.0 μmol h^{-1} g^{-1}, which represented an 8.6 times improvement compared to the activity of pristine CN, resulting in an AQY of 14.5% at 405 nm. The achieved performance was also superior to most previously reported CN-based materials. The mechanism of B-doping-accelerated photocatalytic H_2 evolution over BCN was well elucidated. The combination of experimental and theoretical results revealed that B-doping induced π-electron delocalization in the conjugated CN rings to generate a new intermediate state within the band gap to provide a new transfer pathway for visible-light utilization, thus achieving a high separation and transfer of photoinduced carriers. The

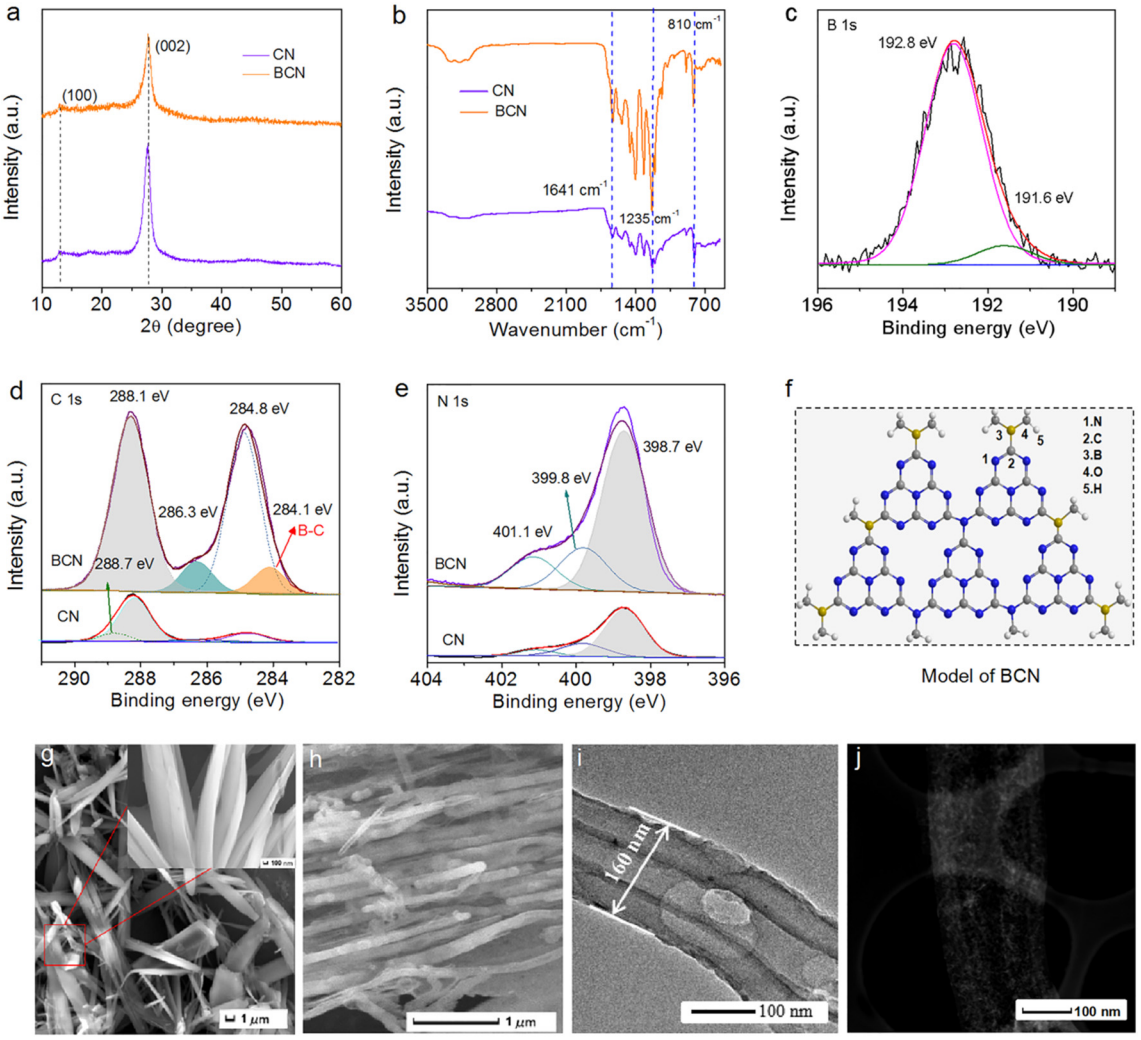

Fig. 1 Comparison of (a) XRD patterns, (b) FT-IR spectra and XPS spectra of CN and BCN: (c) B 1s, (d) C 1s, and (e) N 1s; (f) schematic of the molecular structure of BCN; (g) SEM images of the BCN precursors; (h) SEM, (i) TEM and (j) HAADF-TEM images of BCN.

findings encourage a wider investigation of BCN as a catalyst modifier in photocatalytic H_2 evolution and other photocatalytic reactions.

2 Results and discussion

2.1 Structural characterizations

The BCN sample was synthesized through a solvothermal-calcined method using a B-doped supramolecular intermediate as the precursor. The phase structure of BCN was studied by XRD characterization. As presented in Fig. 1a, the two characteristic XRD peaks at 13.1° (100) and 27.7° (002) were assigned to the diffraction peaks of CN, corresponding to in-plane repeating units and the interlayer stacking of π-conjugated aromatic rings, respectively.[36,37] Compared to CN, the weakened intensity of the (002) peak implied the decreased size of the interlayer over BCN, which was well consistent with previous reports.[38,39] The effect of B-doping on CN was further investigated by FT-IR spectra. Fig. 1b shows a characteristic peak at 810 cm^{-1} corresponding to the breathing vibration mode of *s*-triazine rings.[40] The strong vibration peaks at about 1242, 1327, 1413, and 1641 cm^{-1} were ascribed to the C–N and C=N vibration modes in the conjugated heterocycle system.[41] The broad peaks from about 3000–3600 cm^{-1} were related to O–H or N–H stretching vibration, attributed to the surface adsorbed H_2O or the terminal amino groups.[42] Above all, BCN presented the same vibration peaks as CN. Based on the above results, the introduction of the B element did not change the typical framework structure of CN.

The surface chemical compositions in BCN were further investigated by XPS analysis. The XPS survey spectrum showed that an obvious B peak emerged beside the peaks for the C, N, and O signals (Fig. S3†). BCN had an atomic content of 4.0 at% of B element (Table S1†). In the high-resolution B 1s spectrum (Fig. 1c), the spectrum could be deconvolved into two peaks at 192.8 and 191.6 eV, corresponding to BC_3 and BCO_2, respectively.[43] In the C 1s spectra (Fig. 1d), the BCN sample showed a new peak at 284.1 eV compared with CN, which corresponded to C–B bonds.[44] For the N 1s spectrum of the CN sample (Fig. 1e), the peaks at 398.7, 399.8, and 401.1 eV were assigned to pyridinic nitrogen (C–N=C), tertiary nitrogen ($N–C_3$), and the noncondensing amino group (C–N–H), respectively.[2,24] Both the N 1s and O 1s spectra of the BCN catalyst showed the same XPS spectra as CN (Fig. S4†). Therefore, it could be concluded that the introduction of B atoms only combined with C atoms to form B–C bonds in the BCN catalyst. Based on the reported CN structure,[25–28] the schematic of a perfect model of the BCN photocatalyst is presented in Fig. 1f. Also SEM and TEM images were collected to observe the transformation of the morphology from the intermediate to the final BCN. As shown in Fig. 1g, the supramolecular precursors presented rod-like features and were intertwined (see the inset in Fig. 1g). The element dispersive spectroscopy (EDS) mapping (Fig. S5†) indicated that B, C, and N elements

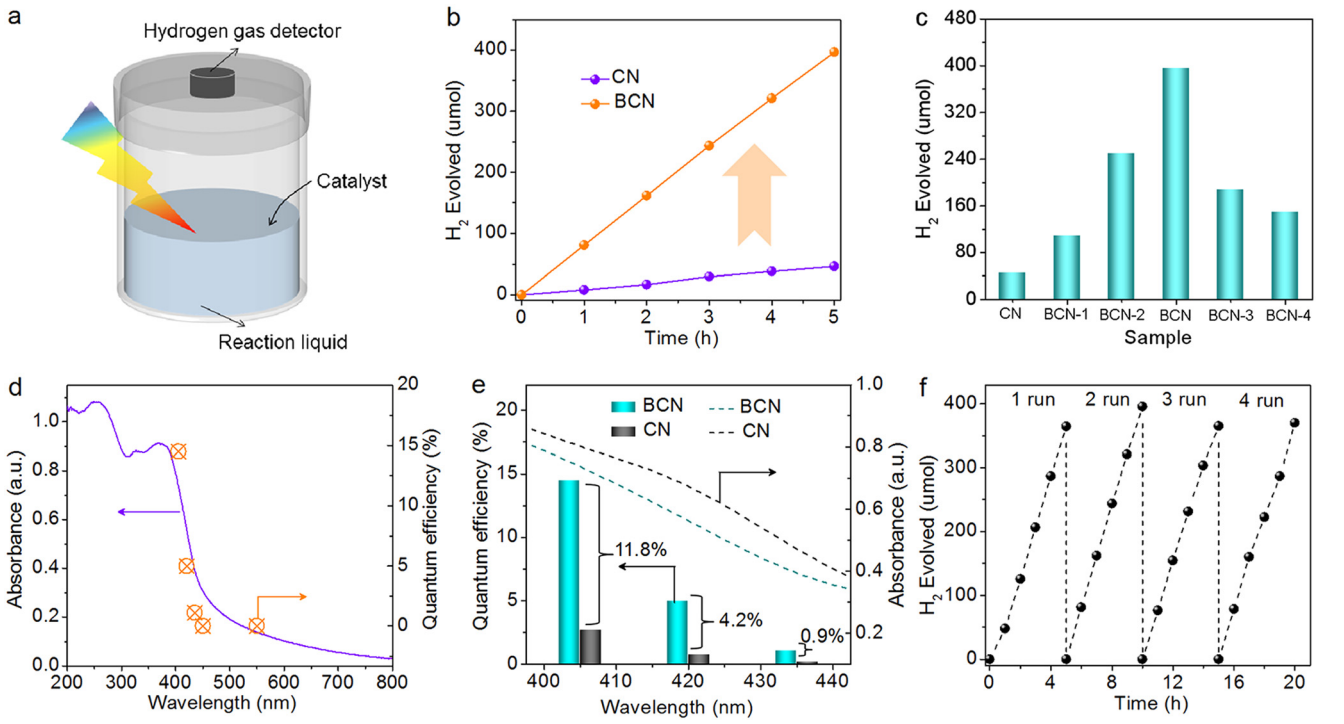

Fig. 2 (a) Schematic of the photocatalytic H_2 evolution device; (b) photocatalytic H_2 evolution of CN and BCN; (c) BCN samples with different B contents, with 10% triethanolamine (V/V) as a sacrificial agent and 3 wt% Pt as a co-catalyst; (d) wavelength dependence of the apparent quantum yield for BCN; (e) comparison of external quantum efficiency for CN and BCN under different single wavelengths; and (f) stability test of photocatalytic H_2 evolution.

were uniformly dispersed onto the BCN catalyst surface. After the thermal polymerization, the obtained BCN catalyst presented a regular tubular structure (Fig. 1h); a single tube with a diameter of ~160 nm could be clearly seen in the TEM image (Fig. 1i), which was further verified by HAADF-TEM (Fig. 1j). The above-mentioned results indicated that the rod-like intermediate was transformed into a regular tubular structure. Moreover, the regular tubular structure of BCN exhibited a large specific surface area (118.7 m^2 g^{-1}) (Fig. S6†), which may provide more active sites and adsorption sites.

2.2 Activity of BCN compared to pristine CN

Photocatalytic H_2 evolution was performed to evaluate the photocatalytic activity of the BCN catalysts. A schematic of the photocatalytic H_2-evolution device is presented in Fig. 2a. Once the catalyst was introduced into the device, a significant quantity of H_2 appeared, which was detected by the H_2-gas detector. As shown in Fig. 2b, 396.2 μmol of H_2 appeared under continuous light irradiation for 5 h for BCN, while the CN showed much lower H_2 production (46.3 μmol) with 3 wt% Pt as a co-catalyst (note: the catalyst showed poor photocatalytic activity in the absence of the co-catalyst (Fig. S7†)). The average amount of BCN was 7924.0 μmol h^{-1} g^{-1}, which represented an 8.6-fold improvement compared to the pristine CN (926.6 μmol h^{-1} g^{-1}). This result suggests that the addition of B can enhance the photocatalytic H_2-evolution performance. Adjusting the amount of B introduced could also affect the quantity of H_2 produced (Fig. 2c). When the B content was 5%, the optimal hydrogen-production performance was achieved. In addition, the optimal BCN catalyst exhibited an apparent quantum yield (AQY) of 14.5% at 405 nm, far superior to that of CN (2.7%) (Fig. 2d). The AQY decreased with elongation of the single wavelength, and the corresponding values were 5.0%, 1.1%, and 0.0% at 420, 435, and 450 nm, respectively (Table S2†). These results were consistent with the optical absorption intensity of the BCN photocatalyst, verifying that the photocatalytic H_2 evolution was driven by light excitation. A comparison of AQY at different wavelengths over BCN and CN was carried out (Fig. 2e). It was found that the gap in AQYs for the as-prepared two catalysts widened from 0.9% to 11.8% with the wavelength decreasing, but the light-absorbing ability of CN was still stronger than that of BCN across this optical cross-section. This was because the improved separation of photoinduced e^-–h^+ pairs on the BCN catalyst might play a primarily role in the enhanced photocatalytic H_2 evolution rather than the intensive light absorption. In addition, the BCN catalyst presented a turnover number (TON) of 257.7, which was 8.6 times that of the pristine CN catalyst (30.1) (Fig. S8 and Table S3†). The achieved performance outperformed most the reported C_3N_4 materials, such as P-doped C_3N_4 tubes (67 μmol h^{-1} g^{-1}),[39] C-rich C_3N_4 nanosheets (39.6 μmol h^{-1} g^{-1}),[45] and 3D porous C_3N_4 (60.2 μmol h^{-1} g^{-1})[46] (Table S4†). The stability of the BCN catalyst was investigated by cycling tests. As shown in Fig. 2f, no noticeable decrease in photocatalytic H_2 evolution was

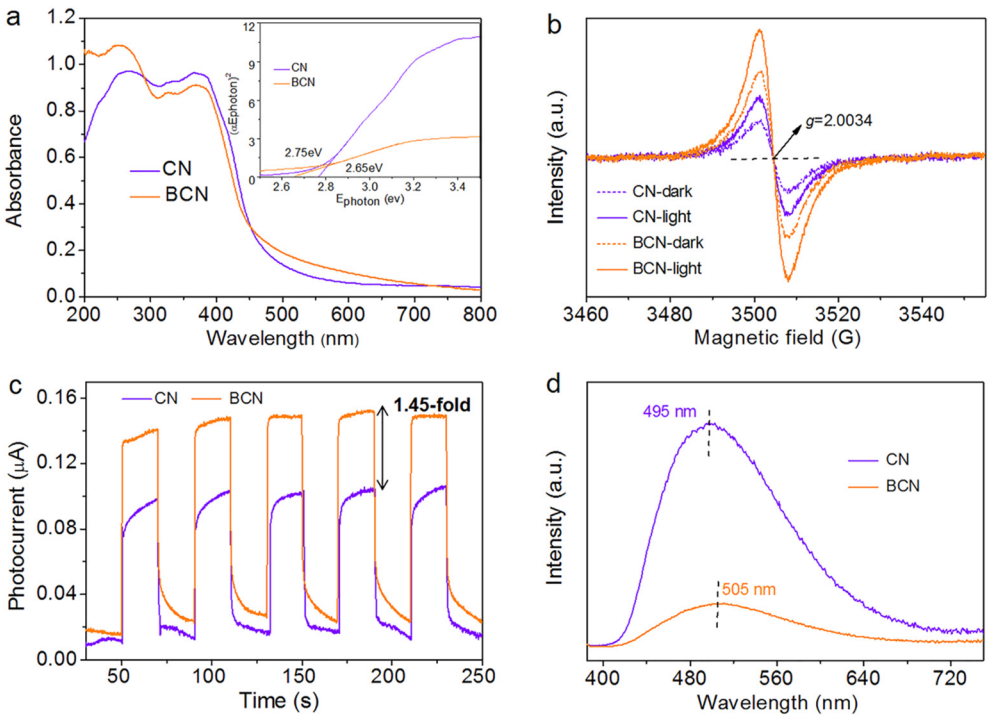

Fig. 3 (a) UV-vis spectra (the inset shows the Tauc/Davis–Mott plots used to estimate band gap energies); (b) room-temperature EPR spectra in the dark and under visible light irradiation; (c) photocurrent response and (d) photoluminescence (PL) spectra of CN and BCN catalysts (photoluminescence was excited by an incident illumination of 375 nm).

detected during the continuous reaction. The structure of the used BCN catalyst (after 20 h testing) was characterized by XRD and FT-IR combined with TEM characterizations (Fig. S9†). Both the morphology and the typical CN framework structure of the used BCN catalyst showed no change in comparison to the fresh BCN catalyst, validating the robust photocatalytic stability of BCN.

2.3 B-doping enhanced separation efficiency of photoinduced e^-–h^+ pairs

Since light absorption affected the photocatalytic activity, ultraviolet-visible (UV-vis) spectroscopy was used to study the sample's light-absorption property. As shown in Fig. 3a, the BCN photocatalyst demonstrated enhanced absorption for visible light relative to CN, which was mainly due to the n → π* electronic transition from the effect of B-doping.[47] The band gap energy (E_g) was estimated by processing the Tauc/Davis–Mott plots based on the Kubelka–Munk function.[10] After introducing the B element, the absorption edge generated a red-shift resulting in a decreased E_g (the value decreased from 2.75 eV to 2.65 eV, see the inset in Fig. 3a). To further reveal the change, both the valence band (VB) and conduction band (CB) were investigated by VB-XPS analysis (Fig. S10†). The VB showed no shift (*ca.* 1.99 eV), while the CB level moved down. This result illustrates that B-doping did not change the VB but reduced the CB. Based on electrochemical Mott–Schottky tests (Fig. S11†), the CB position of BCN was found to be −1.55 eV. The decreased CB facilitates the excited electrons transition under light irradiation. The mobile electron from the occupied orbitals of VB to the unoccupied orbitals in the CB could be described by the room-temperature electron paramagnetic resonance (EPR) spectrum.[23] As shown in Fig. 3b, both the EPR spectra of BCN and CN showed one single Lorentzian line with a g value of 2.0034, which was attributed to the delocalized electrons in π-conjugated CN aromatic rings.[24] Significantly, the EPR signal of BCN was much stronger than that of CN, which manifested the fact that B-doping modulated the electronic structure of the CN framework, generating more delocalized electrons. Under light irradiation, the EPR signals of BCN and CN were further strengthened compared to in the dark, which proved that light can induce the separation of e^-–h^+ pairs. In particular, the enhanced EPR signal of BCN was much higher than that of CN, indicating that B-doping can generate a more efficient separation of photoinduced e^-–h^+ pairs.

The photoelectrochemical characters of the catalysts were tested to unravel the reasons for the enhanced photocatalytic H_2 evolution with the BCN catalyst. The photocurrent response and photoluminescence (PL) spectroscopy were adopted to detect the separation efficiency of the photoinduced charges therein. Compared to CN, BCN showed a larger transient photocurrent and better stability during intermittent illumination (Fig. 3c). Notably, the photocurrent of BCN showed a 1.45-fold enhancement compared with that of CN, and it also presented weaker PL signals (Fig. 3d). These results suggest that the BCN catalyst possesses a higher separation efficiency of photoinduced e^-–h^+ pairs, leading to generating more free photoelectrons to catalyze H_2O splitting and to release H_2 gas. It is worth noting that an obvious red-shift emission peak appeared in the PL spectrum of BCN (505 nm) compared to in the spectrum of CN (495 nm), which was in good agreement with the red-shift of the optical absorption band edge. Furthermore, the fitted parameters of the equivalent circuit showed that BCN (R_2 = 71.9 Ω) had a much smaller resistance (charge-transfer resistance) than that of CN (R_2 = 105.4 Ω) based on the EIS results (Fig. S12a†), which indicates that BCN possessed a faster electron-transfer ability to promote charge transfer to reaction sites. Both the superior separation efficiency of photoinduced e^-–h^+ pairs and fast electron-transfer ability can efficiently facilitate photocatalytic H_2 evolution.[39] Moreover, the fluorescence lifetime (FL) spectra showed the fluorescence lifetimes were 9.38 ns and 15.60 ns over CN and BCN at room temperature, respectively (Fig. S12b†). The enhanced FL provides a greater possibility for photogenerated charge carriers to participate in catalytic reactions. A schematic diagram of the photocatalytic H_2 evolution is exhibited in Fig. S13.† In this process, (step I) the BCN catalyst is stimulated to form photoinduced e^-–h^+ pairs:

$$\mathrm{BCN} + h\nu \rightarrow \mathrm{BCN}^* + \mathrm{e}^- + \mathrm{h}^+ \quad (1)$$

Next, (step II) the generated photoelectrons under visible-light irradiation quickly transfer to the catalytic reaction sites on the BCN surface; (step III) the photoexcited electrons efficiently couple with H+ to generate H_2:

$$\mathrm{H}^+ + \mathrm{e}^- \rightarrow \mathrm{H}_2\uparrow \quad (2)$$

2.4 Formation of the delocalization of π-electrons within conjugated CN aromatic rings

To deeply understand the enhanced photocatalytic H_2 evolution, DFT calculations were carried out to study the effect of B-doping on the electronic structure of the π-conjugated CN aromatic rings. The atomic models of CN and BCN were first built (Fig. S15†). Additional charge caused by electron loss and gain could be uniformly distributed to the π-conjugated CN aromatic rings due to electron delocalization.[48] The charge density distribution showed that the conjugated CN rings gain electrons from B atoms, and the non-uniform dispersion of charge density indicated the delocalization of electrons in the π-conjugated rings of CN (Fig. 4a and Table S5†). Estimated by Bader charge analysis,[49–51] the conjugated CN rings of a unit cell obtained 1.07 e^- from the B atom in total, which was conducive to modulating the electronic structure of CN's π-conjugated rings and then inducing its π-electron delocalization (Fig. S16†). The delocalized electron improves

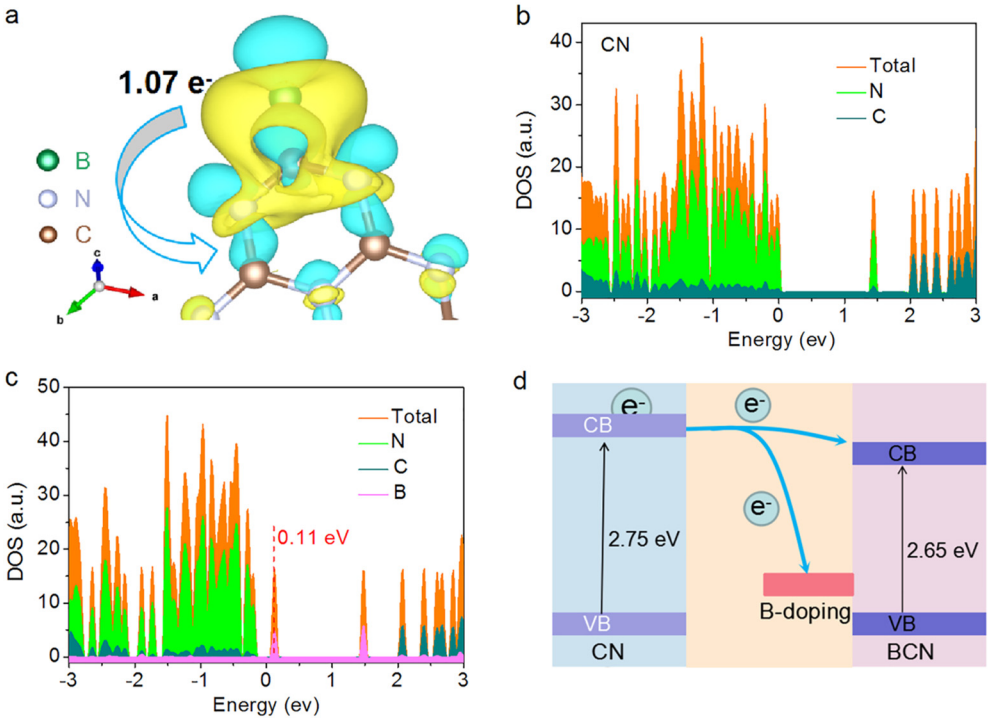

Fig. 4 (a) Difference in charge density for BCN, where charge density in yellow and light blue represent the concentrated and scarce electrostatic potential scale, respectively; (b and c) calculated DOSs, showing the introduction of B can modify the electronic structure of the π-conjugated CN system; (d) schematic band structure evolution of the pristine CN and BCN catalysts.

the dynamics of electron transfer, which provides the possibility for a high separation efficiency of photoinduced e^-–h^+ pairs. Besides, the electron densities of states (DOS) of the two samples were simulated to study the electronic structure. As shown in Fig. 4b and c, the two catalysts presented a typical semiconductor character due to the existence of a band gap. Notably, the introduction of B atoms induced a new intermediate state located at ~0.11 eV above the valence band. The new intermediate energy level within the energy gap has been reported to allow the electrons to be more easily excited into the CB under the same light irradiation, thus achieving a higher solar energy efficiency.[52] Therefore, the introduction of B increased the mobile electrons and promoted a higher separation efficiency of photoinduced e^-–h^+ pairs, which was also in good agreement with the photoelectrochemical characterization analysis. The influence of B-doping on the band structure of the BCN catalyst is presented in Fig. 4d. The band gap of the BCN catalyst narrowed after the introduction of B atoms. The narrowed band gap corresponded to an expanded visible-light adsorption and lowered overpotential for reduction reactions. The more positive CB of BCN, which consisted mainly of carbon p_z orbitals, reduced the thermionic emission of charge transfer caused by the height of the Schottky barrier in the BCN–Pt contact,[53] which accelerates the dynamics of electron transfer to the catalytic reaction sites. Moreover, the accelerated electron-transfer kinetics promoted the formation of superoxide radicals (Fig. S16†).

Based on the above-mentioned results, the reasons for the excellent catalytic performance of the BCN photocatalyst are summarized as follows. First, the introduction of B atoms into the π-conjugated CN system can induce electron delocalization and then facilitate the charge transfer, thus enhancing the separation efficiency of photoinduced e^-–h^+ pairs, as demonstrated by the photocurrent response and PL results. Second, the B dopant produces a new intermediate state within the band gap, where the new intermediate state creates a novel transfer path for visible-light utilization.[28] The enhanced light absorption is favorable to produce more charge carriers. The positive shift of the CB edge lowers the reaction energy barrier of electron transfer, which facilitates the separated photoelectrons quickly transferring to the reaction interface connected with H^+ to release H_2 gas. In other words, B-doping in to the π-conjugated system of CN both induces electron delocalization and facilitates the separation of photoinduced e^-–h^+ pairs, achieving an 8.6-fold improvement in photocatalytic H_2 evolution.

3 Conclusion

In summary, the effect and mechanism of B-doping-induced π-electron delocalization in the π-conjugated CN framework for promoting efficient photocatalytic H_2 evolution is elucidated in depth. The as-prepared BCN photocatalyst presented an 8.6-fold improvement in H_2-evolution rate (7924 μmol h^{-1} g^{-1}) compared to pristine CN. This study

emphasizes the role of a well-designed BCN photocatalyst in promoting the delocalization of π-electrons within conjugated CN aromatic rings. Consequently, B-doping facilitated the efficient transfer of photoinduced electrons to active sites. In particular, the introduction of B atoms into the π-conjugated CN system could capture more incident photons and facilitate the separation of photoinduced e^-–h^+ pairs, achieving a much-improved utilization efficiency of photocarriers. The present study may pave the way toward a rational synthetic approach for designing efficient and low-cost photocatalysts for catalytic energy conversion.

4 Experimental section

4.1 Materials

Melamine (>99.0%) and boric acid (H_3BO_3) (>99.0%) were purchased from Sinopharm Chemical Reagent Co., Ltd., (China). Deionized water was used throughout the entire experimental process.

4.2 Syntheses of BCN and CN

The BCN sample was prepared by a solvothermal–calcination method. First, the intermediate was prepared by molecular self-assembly through coupling with hydrogen bonding between H_3BO_3 and melamine (Fig. S1 and S2,† details of the synthesis and characterization are discussed in the ESI†). After thermal polycondensation by calcining the intermediate, the BCN photocatalyst was successfully obtained (the yield was ~20%). In detail, both H_3BO_3 and melamine (mass ratio of 1 : 20) were dispersed into 18 mL of deionized water under continuous magnetic agitation (500 r min^{-1}, 30 min) to form a suspension. The suspension was then transferred in to a 20 mL autoclave with a polytetrafluoroethylene liner and a high pressure resistant steel sleeve, which was heated at 200 °C in a drying oven and held for 10 h. After washing by centrifugation (12 000 r min^{-1}, 4 min) using deionized water and ethanol three times, respectively, the precipitation was collected, and then dried at 60 °C for 6 h in a drying oven. Next, the dry precipitation was placed in an alumina crucible covered by an aluminum foil and calcined at 550 °C at a ramp rate of 2 °C min^{-1} in a muffle furnace and then kept there for 4 h, in which the heating procedures refer to previous reports.[54,55] The final sample was named as BCN. In addition, 2.0 g melamine was directly calcined using the same method as for the BCN. The synthesized sample was denoted as CN, which was the control sample.

4.3 Photocatalytic H_2-evolution test

The photocatalytic H_2-evolution test was carried out on an online monitoring system (LabSolar-IIIAG, PerfectLight, Beijing). First, 10 mg sample was added to a mixed solution consisting of 90 mL deionized water and 10 mL triethanolamine. Then, 3 wt% $H_2PtCl_6{\cdot}6H_2O$ was added to form a uniform suspension by sonication for 5 min. The reactor was fixed on the online monitoring system under continuous stirring. Next, the system, which was vacuumed to specific negative pressure, was irradiated using a 300 W xenon lamp (PLS-SXE 300C (BF), PerfectLight, Beijing) with an optical filter ($\lambda > 400$ nm). The top of the reactor was in close contact with the bottom of the xenon lamp. A cooling system kept at 15 °C was adopted to take away the heat produced by the absorption of light energy. The evolved H_2 was detected by an online gas chromatography system (GC D7900P, TCD detector). The cycling tests were also carried out using the above similar method. In particular, the system was vacuumed after each test. Immediately, the photocatalyst was collected by centrifugation for analysis to assess the structure and performance stability.

The photocatalytic H_2 production amount and the rate could be calculated as follows:

$$Y = \frac{V}{22.4 \times 1000} \tag{3}$$

$$v = \frac{Y}{m \times t} \tag{4}$$

where Y represents H_2 production (μmol), V is the volume of H_2 (mL), v represents the H_2-production rate (μmol h^{-1} g^{-1}), m is the mass of sample (g), and t is the reaction time (h).

The apparent quantum yield (AQY) was calculated as follows:

$$N = \frac{E\lambda}{hc} \tag{5}$$

$$\mathrm{AQY} = \frac{N_r}{N} \tag{6}$$

where N represents the number of incident photons, N_r represents the number of reacted photons, E represents the light intensity (mW), λ is the wavelength of incident light (nm), h is the Planck constant, and c is the speed of light (3×10^8 m s^{-1}).

4.4 Characterization

The powder X-ray diffraction (XRD) patterns were obtained on a Bruker D8 diffractometer with Cu Kα radiation (λ = 1.5418 Å) in the range of 2Θ = 10–60°. The transmission electron microscopy (TEM) images were collected on a JEOL-JEM-2010 instrument (JEOL, Japan) operated at 200 kV. The Fourier transform infrared spectra (FT-IR) were recorded on a Nicolet Nexus 470 spectrometer (Nicolet 6700, Thermo Scientific, USA). X-Ray photoelectron spectroscopy (XPS) tests were performed on an ESCALab MKII X-ray photoelectron spectrometer using Al Kα radiation (ESCALAB 250, Thermo Scientific, USA). The ultraviolet-visible (UV-vis) diffuse reflection spectra of the samples were obtained with a UV-vis spectrophotometer (Shimadzu UV-2450, Japan) in the range

of 200–800 nm, then converted into absorption spectra by Kubelka–Munk formula transformation, with $BaSO_4$ used as a standard reflectance material. The room-temperature electron paramagnetic resonance (EPR) measurements were performed on an EPR spectrometer (JES-FA 200, JEOL, Japan) with a modulation frequency of 100 kHz and a microwave power of 1.0 mW. A 300 W xenon lamp with a cut-off filter ($\lambda > 400$ nm) was adopted as the illumination source for the *in situ* EPR measurements. The photoluminescence (PL) emission spectra were recorded on a Quanta Master and Time Master spectrofluorometer excited by incident illumination of 375 nm. The electrochemical measurements were performed on an electrochemical station (CHI 660E, CH instruments, China). A standard three-electrode system, consisting of a platinum wire as the counter electrode, indium tin oxide (ITO) glass as the working electrode, and Ag/AgCl (saturated KCl solution) as the reference electrode, was adopted. All the photocurrent measurements were performed at a constant potential of −0.2 V (*vs.* Ag/AgCl). Phosphate buffer solution (PBS) (0.1 M, pH = 7.0) was used as the electrolyte for the photocurrent measurements. A 300 W xenon lamp was utilized as the light source. Electrochemical impedance spectroscopy (EIS) analysis was carried out in 0.1 M potassium chloride solution containing 5 mM ferricyanide/ferrocyanide in the frequency range from 0.01 Hz to 10 kHz at 0.24 V, and the amplitude of the applied sine wave potential in each case was 5 mV. Here, 1 mg of the sample was dispersed ultrasonically in 1 mL deionized water, and 20 μL of the obtained colloidal dispersion (1 mg mL^{-1}) was then drop-cast onto a piece of ITO with a fixed area of 0.5 cm^2, and dried under an infrared lamp to form the sample-modified ITO electrode.

Data availability

The data supporting this article have been included as part of the ESI.†

Author contributions

Quanguo Hao: conceptualization, methodology, data curation, validation, writing – original draft. Yuhua Zhu: validation, investigation, writing – review & editing. Yuan Li: validation, investigation. Zhenhua Li: conceptualization, methodology, investigation, writing – review & editing, supervision. Hong Yuan: validation, investigation. Shuxin Ouyang: resources, project administration, funding acquisition.

Conflicts of interest

The authors declare that they have no known competing financial interests or personal relationships that could have appeared to influence the work reported in this paper.

Acknowledgements

The authors acknowledge the financial support from the National Key Projects for Fundamental Research and Development of China (2021YFA1500803), the National Natural Science Foundation of China (No. 22209190), the Central China Normal University (2020CXZZ023), the Young Elite Scientists Sponsorship Program by CAST (2023QNRC001) and the Beijing Natural Science Foundation (2222081). S. O. appreciates the financial support from the "Guizi Scholar" Program of Central China Normal University and the fellowship of China Postdoctoral Science Foundation (No. GZC20241766, 2024M753304).

References

1 W. Che, W. Cheng, T. Yao, F. Tang, W. Liu, H. Su, Y. Huang, Q. Liu, J. Liu, F. Hu, Z. Pan, Z. Sun and S. Wei, Fast photoelectron transfer in (Cring)-C_3N_4 plane heterostructural nanosheets for overall water splitting, *J. Am. Chem. Soc.*, 2017, **139**, 3021–3026.
2 Y. Bao, S. Du, K. Shibata, X. Guo, Y. Kamakura, Z. Feng, Y. Huang, O. Ishitani, K. Maeda and F. Zhang, Layered β-ZrNBr nitro-halide as multifunctional photocatalyst for water splitting and CO_2 reduction, *Angew. Chem., Int. Ed.*, 2023, e202214273.
3 C. Ponseca, J. Chabera, J. Uhlig, P. Persson and V. Sundstrom, Ultrafast electron dynamics in solar energy conversion, *Chem. Rev.*, 2017, **117**, 10940–11024.
4 Y. Qi, B. Zhang, G. Zhang, Z. Zheng, T. Xie, S. Chen, G. Ma, C. Li, K. Domen and F. Zhang, Efficient overall water splitting of a suspended photocatalyst boosted by metalsupport interaction, *Joule*, 2024, **8**, 193–203.
5 J. Gong, C. Li and M. Wasielewski, Advances in solar energy conversion, *Chem. Soc. Rev.*, 2019, **48**, 1862–1864.
6 L. Wang, J. Liu, H. Wang, H. Cheng, X. Wu, Q. Zhang and H. Xu, Forming electron traps deactivates self-assembled crystalline organic nanosheets toward photocatalytic overall water splitting, *Sci. Bull.*, 2021, **66**, 265–274.
7 L. Xie, X. Wang, Z. Zhang, Y. Ma, T. Du, R. Wang and J. Wang, Photosynthesis of hydrogen peroxide based on g-C_3N_4: The road of a cost-effective clean fuel production, *Small*, 2023, **19**, 2301007.
8 S. Chen, T. Takata and K. Domen, Particulate photocatalysts for overall water splitting, *Nat. Rev. Mater.*, 2017, **2**, 17050–17066.
9 F. Tian, X. Huang, W. Li, Y. An, G. Li and R. Chen, Weak interaction between nickel thiolate and g-C_3N_4 improving electron-hole separation for photocatalysis, *ACS Catal.*, 2023, **13**, 12186–12196.
10 Q. Hao, Y. Song, H. Ji, Z. Mo, X. She, J. Deng, T. Muhmood, X. Wu, S. Yuan, H. Xu and H. Li, Surface N modified 2D g-C_3N_4 nanosheets derived from DMF for photocatalytic hydrogen evolution, *Appl. Surf. Sci.*, 2018, **459**, 845–852.
11 C. Zhao, Z. Chen, R. Shi, X. Yang and T. Zhang, Recent advances in conjugated polymers for visible-light-driven water splitting, *Adv. Mater.*, 2020, 1907296.

12 S. Patnaik, D. P. Sahoo and K. Parida, Recent advances in anion doped g-C_3N_4 photocatalysts: A review, *Carbon*, 2021, **172**, 682–711.
13 Y. Xiao, G. Tian, W. Li, Y. Xie, B. Jiang, C. Tian, D. Zhao and H. Fu, Molecule self-assembly synthesis of porous few-layer carbon nitride for highly efficient photoredox catalysis, *J. Am. Chem. Soc.*, 2019, **141**, 2508–2515.
14 K. L. Corp and C. W. Schlenker, Ultrafast spectroscopy reveals electron-transfer cascade that improves hydrogen evolution with carbon nitride photocatalysts, *J. Am. Chem. Soc.*, 2017, **139**, 7904–7912.
15 Y. Wang, R. Godin, J. Durrant and J. Tang, Efficient hole trapping in carbon dot/oxygen-modified carbon nitride heterojunction photocatalysts for enhanced methanol production from CO_2 under neutral conditions, *Angew. Chem., Int. Ed.*, 2021, **60**, 20811–20816.
16 X. Xiao, Y. Gao, L. Zhang, J. Zhang, Q. Zhang, Q. Li, H. Bao, J. Zhou, S. Miao, N. Chen, J. Wang, B. Jiang, C. Tian and H. Fu, A promoted charge separation/transfer system from Cu single atoms and C_3N_4 layers for efficient photocatalysis, *Adv. Mater.*, 2020, **32**, 2003082.
17 E. Cao, Z. Chen, H. Wu, P. Yu, Y. Wang, F. Xiao, S. Chen, S. Du, Y. Xie, Y. Wu and Z. Ren, Boron-induced electronic-structure reformation of CoP nanoparticles drives enhanced PH-universal hydrogen evolution, *Angew. Chem., Int. Ed.*, 2020, **59**, 4154–4160.
18 Y. Gong, J. Lin, X. Wang, G. Shi, S. Lei, Z. Lin, X. Zou, G. Ye, R. Vajtai, B. I. Yakobson, H. Terrones, M. Terrones, B. K. Tay, J. Lou, S. T. Pantelides, Z. Liu, W. Zhou and P. M. Ajayan, Vertical and in-plane heterostructures from WS_2/MoS_2 monolayers, *Nat. Mater.*, 2014, **13**, 1135–1142.
19 V. W. Lau, M. B. Mesch, V. Duppel, V. Blum, J. Senker and B. V. Lotsch, Low-molecular-weight carbon nitrides for solar hydrogen evolution, *J. Am. Chem. Soc.*, 2015, **137**, 1064–1072.
20 M. Zhu, S. Kim, L. Mao, M. Fujitsuka, J. Zhang, X. Wang and T. Majima, Metal-free photocatalyst for H_2 evolution in visible to near-infrared region: Black phosphorus/graphitic carbon nitride, *J. Am. Chem. Soc.*, 2017, **139**, 13234–13242.
21 H. Yu, R. Shi, Y. Zhao, T. Bian, Y. Zhao, C. Zhou, G. Waterhouse, L. Wu, C. Tung and T. Zhang, Alkali-assisted synthesis of nitrogen deficient graphitic carbon nitride with tunable band structures for efficient visible-light-driven hydrogen evolution, *Adv. Mater.*, 2017, **29**, 1605148.
22 V. Lau, I. Moudrakovski, T. Botari, S. Weinberger, M. Mesch, V. Duppel, J. Senker, V. Blum and B. Lotsch, Rational design of carbon nitride photocatalysts by identification of cyanamide defects as catalytically relevant sites, *Nat. Commun.*, 2016, **7**, 12165–12174.
23 J. Ning, B. Zhang, L. Siqin, G. Liu, Q. Wu, S. Xue, T. Shao, F. Zhang, W. Zhang and X. Liu, Designing advanced S-scheme CdS QDs/La-Bi_2WO_6 photocatalysts for efficient degradation of RhB, *Exploration*, 2023, **3**, 20230050.
24 Z. Lan, G. Zhang and X. Wang, A facile synthesis of Br-modified g-C_3N_4 semiconductors for photoredox water splitting, *Appl. Catal., B*, 2016, **192**, 116–125.
25 Y. Zheng, Z. Yu, F. Lin, F. Guo, K. Alamry, L. Taib, A. Asiri and X. Wang, Sulfur-doped carbon nitride polymers for photocatalytic degradation of organic pollutant and reduction of Cr (VI), *Molecules*, 2017, **22**, 572–588.
26 Y. Wang, H. Wang, F. Chen, F. Cao, X. Zhao, S. Meng and Y. Cui, Facile synthesis of oxygen doped carbon nitride hollow microsphere for photocatalysis, *Appl. Catal., B*, 2017, **206**, 417–425.
27 D. Zhao, Y. Wang, C. Dong, Y. Huang, J. Chen, F. Xue, S. Shen and L. Guo, Boron-doped nitrogen-deficient carbon nitride-based Z-scheme heterostructures for photocatalytic overall water splitting, *Nat. Energy*, 2021, **6**, 388–397.
28 M. Jerigova, Y. Markushyna, I. F. Teixeira, B. Badamdorj, M. Isaacs, D. Cruz, I. Lauermann, M. Á. Muñoz-Márquez, N. V. Tarakina, N. López-Salas, O. Savateev and P. Jimenéz-Calvo, Green light photoelectrocatalysis with sulfur-doped carbon nitride: Using triazole-purpald for enhanced benzylamine oxidation and oxygen evolution reactions, *Adv. Sci.*, 2023, **10**, 2300099.
29 Y. Shang, M. Zheng, H. Liu, X. Jin, C. Yan, L. Song, Z. Qi, F. Jing, P. Song, X. Zhou, G. Chen and C. Lv, Mimicking frustrated lewis pairs on graphitic carbon nitride for CO_2 photoreduction, *ACS Catal.*, 2023, **13**, 14530–14539.
30 J. Wu, M. Rodrigues, R. Vajtai and P. Ajayan, Tuning the electrochemical reactivity of Boron- and Nitrogen-substituted graphene, *Adv. Mater.*, 2016, **28**, 6239–6246.
31 M. Jing, H. Zhao, L. Jian, C. Pan, Y. Dong and Y. Zhu, Coral-like B-doped g-C_3N_4 with enhanced molecular dipole to boost photocatalysis-self-fenton removal of persistent organic pollutants, *J. Hazard. Mater.*, 2023, **449**, 131017.
32 P. Giusto, H. Arazoe, D. Cruz, P. Lova, T. Heil, T. Aida and M. Antonietti, Boron carbon nitride thin films: from disordered to ordered conjugated ternary materials, *J. Am. Chem. Soc.*, 2020, **142**, 20883–20891.
33 L. Shi, Z. Zhou, Y. Zhang, C. Ling, Q. Li and J. Wang, Photocatalytic conversion of CO to fuels with water by B-doped graphene/g-C_3N_4 heterostructure, *Sci. Bull.*, 2021, **66**, 1186–1193.
34 D. Zhao, Y. Wang, C. Dong, Y. Huang, J. Chen, F. Xue, S. Shen and L. Guo, Boron-doped nitrogen-deficient carbon nitride-based Z-scheme heterostructures for photocatalytic overall water splitting, *Nat. Energy*, 2021, **6**, 388–397.
35 L. Chen, Y. Wang, S. Cheng, X. Zhao, J. Zhang, Z. Ao, C. Zhao, B. Li, S. Wang, S. Wang and H. Sun, Nitrogen defects/boron dopants engineered tubular carbon nitride for efficient tetracycline hydrochloride photodegradation and hydrogen evolution, *Appl. Catal., B*, 2022, **303**, 120932.
36 G. Zhang, A. Savateev, Y. Zhao, L. Li and M. Antonietti, Advancing the n → π* electron transition of carbon nitride nanotubes for H_2 photosynthesis, *J. Mater. Chem. A*, 2017, **5**, 12723–12728.
37 Y. Li, H. Xu, S. Ouyang, D. Lu, X. Wang, D. Wang and J. Ye, In-situ surface alkalinized g-C_3N_4 toward enhancement of photocatalytic H_2 evolution under visible-light irradiation, *J. Mater. Chem. A*, 2016, **4**, 2943–2950.

38 J. Ding, Q. Tang, Y. Fu, Y. Zhang, J. Hu, T. Li, Q. Zhong, M. Fan and H. H. Kung, Core-shell covalently linked graphitic carbon nitride-melamine- resorcinol-formaldehyde microsphere polymers for efficient photocatalytic CO_2 reduction to methanol, *J. Am. Chem. Soc.*, 2022, **144**, 9576–9585.
39 S. Guo, Z. Deng, M. Li, B. Jiang, C. Tian, Q. Pan and H. Fu, Phosphorus-doped carbon nitride tubes with a layered micro-nanostructure for enhanced visible-light photocatalytic hydrogen evolution, *Angew. Chem., Int. Ed.*, 2016, **55**, 1830–1834.
40 Y. Li, S. Ouyang, H. Xu, W. Hou, M. Zhao, H. Chen and J. Ye, Targeted exfoliation and reassembly of polymeric carbon nitride for efficient photocatalysis, *Adv. Funct. Mater.*, 2019, 1901024.
41 H. Ou, P. Yang, L. Lin, M. Anpo and X. Wang, Carbon nitride aerogels for the photoredox conversion of water, *Angew. Chem., Int. Ed.*, 2017, **56**, 10905–10910.
42 Y. Cui, G. Zhang, Z. Lin and X. Wang, Condensed and low-defected graphitic carbon nitride with enhanced photocatalytic hydrogen evolution under visible light irradiation, *Appl. Catal., B*, 2016, **181**, 413–419.
43 Q. Hao, Z. Li, Y. Shi, R. Li, Y. Li, S. Ouyang, H. Yuan and T. Zhang, Boron-doped CN supported metallic Co catalysts with interfacial electron transfer for enhanced photothermal CO hydrogenation, *Nano Energy*, 2022, **102**, 107723.
44 F. Guo, P. Yang, Z. Pan, X. Cao, Z. Xie and X. Wang, Carbon-doped BN nanosheets for the oxidative dehydrogenation of ethylbenzene, *Angew. Chem., Int. Ed.*, 2017, **56**, 8231–8235.
45 K. Wang, Q. Li, B. Liu, B. Cheng, W. Ho and J. Yu, Sulfur-doped g-C_3N_4 with enhanced photocatalytic CO_2-reduction performance, *Appl. Catal., B*, 2015, **176–177**, 44–52.
46 Y. Li, M. Yang, Y. Xing, X. Liu, Y. Yang, X. Wang and S. Song, Preparation of carbon-rich g-C_3N_4 nanosheets with enhanced visible light utilization for efficient photocatalytic hydrogen production, *Small*, 2017, **13**, 1701552.
47 S. An, G. Zhang, K. Li, Z. Huang, X. Wang, Y. Guo, J. Hou, C. Song and X. Guo, Self-supporting 3D carbon nitride with tunable n → π* electronic transition for enhanced solar hydrogen production, *Adv. Mater.*, 2021, **33**, 2104361.
48 Z. Li, Z. Zhang, H. Hu, Q. Liu and X. Wang, Synthesis of two-dimensional polyoxoniobate-based clusterphenes with in-plane electron delocalization, *Nat. Synth.*, 2023, **2**, 989–997.
49 Y. Yao, Y. Zhu, C. Pan, C. Wang, S. Hu, W. Xiao, X. Chi, Y. Fang, J. Yang, H. Deng, S. Xiao, J. Li, Z. Luo and Y. Guo, Interfacial sp C-O-Mo hybridization originated high-current density hydrogen evolution, *J. Am. Chem. Soc.*, 2021, **143**, 8720–8730.
50 J. Yang, K. Yang, X. Zhu, Z. Wang, Z. Yang, X. Ding, K. Zhong, M. He, H. Li and H. Xu, Band engineering of non-metal modified polymeric carbon nitride with broad spectral response for enhancing photocatalytic CO_2 reduction, *Chem. Eng. J.*, 2023, **461**, 141841.
51 J. Yang, X. Zhu, Q. Yu, M. He, W. Zhang, Z. Mo, J. Yuan, Y. She, H. Xu and H. Li, Multidimensional In_2O_3/In_2S_3 heterojunction with lattice distortion for CO_2 photoconversion, *Chin. J. Catal.*, 2022, **43**, 1286–1294.
52 S. Gao, B. Gu, X. Jiao, Y. Sun, X. Zu, F. Yang, W. Zhu, C. Wang, Z. Feng, B. Ye and Y. Xie, Highly efficient and exceptionally durable CO_2 photoreduction to methanol over freestanding defective single-unit-cell bismuth vanadate layers, *J. Am. Chem. Soc.*, 2017, **139**, 3438–3445.
53 J. Chen, L. Zhang, Z. Lam, H. Tao, Z. Zeng, H. Yang, J. Luo, L. Ma, B. Li, J. Zheng, S. Jia, Z. Wang, Z. Zhu and B. Liu, Tunneling interlayer for efficient transport of charges in metal oxide electrodes, *J. Am. Chem. Soc.*, 2016, **138**, 3183–3189.
54 J. Luo, Y. Liu, C. Fan, L. Tang, S. Yang, M. Liu, M. Wang, C. Feng, X. Ouyang, L. Wang, L. Xu, J. Wang and M. Yan, Direct attack and indirect transfer mechanisms dominated by reactive oxygen species for photocatalytic H_2O_2 production on g-C_3N_4 possessing nitrogen vacancies, *ACS Catal.*, 2021, **11**, 11440–11450.
55 Q. Hao, Y. Song, Z. Mo, J. Deng, J. Yi, W. El-Alami, H. Xu and H. Li, Accelerating the hole mobility of graphitic carbon nitride for photocatalytic hydrogen evolution via 2D/2D heterojunction structural advantages and $Ni(OH)_2$ characteristic, *Sol. RRL*, 2020, 1900538.